Article

Fabrication of Mn-TPP/RGO Tailored Glassy Carbon Electrode for Doxorubicin Sensing

Rafia Zafar, Syeda Aqsa Batool Bukhari, and Habib Nasir*

Cite This: *ACS Omega* 2024, 9, 25694−25703

Read Online

ACCESS | Metrics & More | Article Recommendations | SI Supporting Information

ABSTRACT: Cancer is a long-standing disease, and the use of anticancer drugs can cause many different harmful side effects. Therefore, the quantitative analysis of anticancer drugs is crucial. Among all the analytical techniques that have been utilized for the detection of doxorubicin, electrochemical sensors have drawn exceptional consideration because they are simple, affordable, and highly sensitive. Manganese tetraphenylporphyrin decorated reduced graphene oxide (Mn-TPP/RGO), tetraphenylporphyrin decorated reduced graphene oxide (TPP/RGO), and reduced graphene oxide (RGO) nanostructure based glassy carbon electrodes (GCEs) were fabricated for the detection of doxorubicin (DOX). The synthesized materials were characterized by FTIR, scanning electron microscopy (SEM), ultraviolet−visible spectroscopy (UV/vis), energy dispersive X-ray spectroscopy (EDS), and X-ray diffraction (XRD). Doxorubicin detection was performed using differential pulse voltammetry (DPV), electrochemical impedance spectroscopy (EIS), and cyclic voltammetry (CV). Among the prepared electrodes, Mn-TPP/RGO modified GCE gave an optimum peak current at pH 3. The Mn-TPP/RGO modified electrode showed significant linear response range (0.1−0.6 mM); effective sensitivity (112.09 μA mM^{-1} cm^{-2}); low detection limit (63.5 μM); and excellent stability, selectivity, repeatability, and reproducibility toward doxorubicin. With differential pulse voltammetry, LoD and sensitivity were 27 μM and 0.174 μA μM^{-1} cm^{-2}, respectively. Real sample analysis was also performed in human serum, and it depicted reasonable recovery results for spiked doxorubicin.
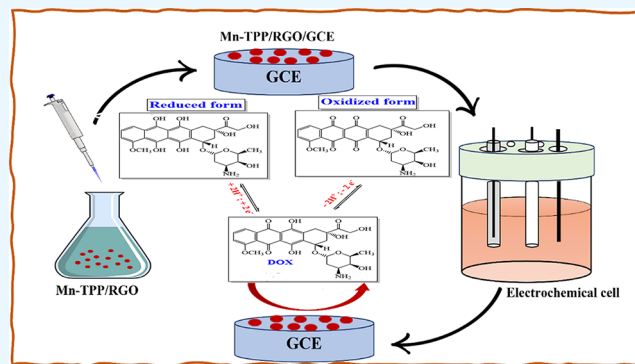
INTRODUCTION

Cancer is a long-term disorder and is considered to be a global epidemic. It is caused by mutation of DNA that results in uncontrollable mitotic divisions of cells. Radiotherapy, chemotherapy and surgery are the main treatments for cancer.[1] However, chemotherapy is widely used to treat cancer by using anticancer drugs that are cytostatic or cytotoxic. Nevertheless, chemotherapy also implies identical effect on normal cells and damage them because drugs are directly introduced in the circulatory system.[2] Anticancer drugs typically intrude with the mitotic division of cells and cause necrosis. Therefore, it is crucial to real-time monitor and control the amount of drug in the blood.[3]

Doxorubicin (DOX), also called hydroxydaunomycin and hydroxydaunorubicin,[4,5] belongs to a class of anticancer drugs called antineoplastics. It has been used for the treatment of many types of cancers like adenocarcinoma, blood cancer, osteosarcoma, gastric cancer, Hodgkin's and non-Hodgkin's lymphomas, carcinomas, and ovarian cancer.[6−10] It has demonstrated potent anticancer effects, as it slows the growth rate of tumor cells by impeding an enzyme called topoisomerase 2. A high dose of doxorubicin is known to cause bone marrow suppression and myocardiopathy,[11] and it can also cause cardiovascular disease leading to death.[12] Thus, it is crucial to monitor the amount of doxorubicin in the blood.

A number of techniques including fluorescence emission spectroscopy,[13] HPLC,[14] capillary electrophoresis,[15] mass spectrometry,[16] UV/vis spectroscopy,[17] Raman spectrometry,[18,19] and electrochemical methods[20] have been used for the detection and determination of anticancer drugs. We opted for the electrochemical method due to its superior characteristics over all other methods. It is a highly sensitive, highly specific, low-cost, fast, and simple method. Moreover, in situ and real-time analysis of analyte can also be performed.[9] In electrochemical sensing, the glassy carbon electrode has been modified with various nanocomposites to increase electron transfer rate, which in turn detects analyte successfully.[18]
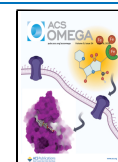
Graphene has a layered structure with free electrons due to which it is applied in many electroanalytical techniques. During different synthesis routes of graphene, many other materials in its family have emerged. The graphene family includes graphene oxide (GO), reduced graphene oxide (RGO), and graphite oxide.[21] Because of its chemical, mechanical, and optical characteristics, reduced graphene oxide has gained much attention for electrochemical analysis. Furthermore, it has a large surface area that supports the stacking of substrates on it by π-π noncovalent interactions.[22] Porphyrin is an organic heterocyclic macromolecule that is composed of four pyrrole rings.[23,24] Owing to its luminescent and electron transfer properties, porphyrin has attracted attention in various fields like electrocatalysis, optical devices, and chemical sensors.[25] Porphyrins can be modified by incorporating various transition metals (Au, Cu, Mn, Zn, etc.)[26−29] that also enhance their electrocatalytic properties.[26] Metalloporphyrins have exhibited excellent electrocatalytic activity for the oxidation and reduction of various compounds[23,24,30] like phenols[31] and hydroquinone.[32]

In this study, RGO was synthesized by graphene oxide, whereas manganese was incorporated in tetraphenylporphyrin to form Mn-TPP. TPP and Mn-TPP were stacked over the RGO by π-π stacking interactions to form the nanocomposites. Synthesized nanocomposites were characterized by XRD, FTIR, UV−vis, EDS, and SEM techniques. Different electrodes were prepared by modification of the glassy carbon electrode (GCE) using different compounds, i.e., RGO, TPP, Mn-TPP, TPP/RGO, and Mn-TPP/RGO. EIS was applied to analyze the charge transfer rate at each electrode. Effective detection of DOX was made possible because of the combined effect of chemoresponsive activity and electron transfer ability of Mn-TPP/RGO. DPV and CV were applied for the electrochemical analysis of DOX.

■ EXPERIMENTAL SECTION

Materials. Graphite powder (≥99.9%), sulfuric acid (95%), sodium nitrate (≥99.9%), hydrochloric acid (37%), glacial acetic acid (99%), pyrrole (96%), potassium ferricyanide (99%), and manganese acetate (98%) were sourced from Sigma-Aldrich, whereas hydrogen peroxide (30%), potassium permanganate (97%), methanol (99%), ethanol (99.8%), chloroform (99%), hydrazine monohydrate (80%), propanoic acid (≥99.5%), and benzaldehyde were sourced from Merck. Doxorubicin was purchased from Zydus Celexa. The stock solution of DOX was formulated by dissolving 25 mg of DOX in 25 mL of deionized water (DI water). Phosphate-buffered solution (PBS) at pH 7 was prepared by using dipotassium hydrogen phosphate (K_2HPO_4) (0.05 M) and potassium dihydrogen phosphate (KH_2PO_4) (0.05 M). Deionized water was used to prepare aqueous solutions. Alumina polish (particle size of 0.05 μm) was used for polishing of the electrode.

Instrumentation. UV/vis analysis of manganese-tetraphenylporphyrin and nanocomposites was performed by a PerkinElmer Lambda 365 instrument in the wavelength range of 300−700 nm. For FTIR analysis, a Bruker Alpha platinum-ATR was used. A Mira3 Tescan scanning electron microscope (SEM) at a working voltage of 20 kV and an energy dispersive X-ray spectrometer (EDS) were employed to determine the morphology and elemental composition of nanocomposites, respectively. The high-performance potentiostat Gamry Reference 3000 was used to carry out electro-

chemical analysis utilizing a three-electrode system in which the reference electrode was Ag/AgCl, the counter electrode was platinum wire, and the working electrode was glassy carbon electrode. For filling of the reference electrode, 3 M KCl solution was used. The potential window was kept between −1 and +1 V vs (Ag/AgCl), whereas the scan rate was 50 mV s^{-1}. The sensitivity of the electrode was estimated by dividing the value of the slope (obtained from the calibration curve between peak current I_{pa} and concentration of analyte DOX) by the electroactive surface area of the electrode. Similarly, the limit of detection (LoD) and limit of quantification (LoQ) were obtained by and 2, respectively.[33]

$$LoD = \frac{3 \times (\text{standard deviation of blank})}{\text{slope obtained from concentration studies of analyte}} \quad (1)$$

$$LoQ = \frac{10 \times (\text{standard deviation of blank})}{\text{slope obtained from concentration studies of analyte}} \quad (2)$$

Methodology. *Synthesis of Manganese(II) Tetraphenylporphyrin.* TPP was synthesized by the Adler−Longo method.[34] Mn-TPP was synthesized by metalation of TPP as reported[35] and as shown in Scheme S1. Briefly, propionic acid (273 mL) along with glacial acetic acid (5 mL) was refluxed, and the mixture of freshly distilled pyrrole (5.09 mL) and benzaldehyde (7.27 mL) was added slowly and further refluxed for 45 min. The reaction mixture was allowed to cool and settle down. The obtained product was filtered and then washed with methanol and DI water and dried at 50 °C to obtain purple crystals of TPP (19%).

For metalation, manganese acetate tetrahydrate ($Mn(OAc)_2 \cdot 4H_2O$) (1395 mg) was dissolved in methanol (30 mL) and added in TPP solution in chloroform (500 mg in 50 mL) (Scheme S2). After refluxing for 6 h, the reaction mixture was cooled, and the solvent was removed under a vacuum though a rotary evaporator. It was filtered and washed with chloroform and then dried in a vacuum oven at 50 °C for 4 h (yield 75%).[28]

Synthesis of Chemically Reduced Graphene Oxide/Manganese(II) Tetraphenylporphyrin Nanocomposite. Graphene oxide (GO) was synthesized by the reported modified Hummers' method.[36] RGO was synthesized by the chemical reduction of graphene oxide as reported.[37] GO (100 mg) was dispersed in 100 mL of deionized water under ultrasonication for 2 h. Hydrazine hydrate (1 mL) was added in the reaction mixture, and the reaction mixture was refluxed for 24 h at 100 °C. The product was separated by centrifugation (at 7000 rpm for 30 min). Then it was dried in a vacuum oven at 50 °C to obtain RGO. To prepare the Mn-TPP/RGO nanocomposite, Mn-TPP (30 mg) was dissolved in chloroform (30 mL) and mixed with RGO (10 mg) dispersed in ethanol (10 mL). The reaction mixture was sonicated for 2 h, and then the suspension was centrifuged (at 6000 rpm for 20 min), washed with ethanol, and dried in vacuum oven at 50 °C to obtain the Mn-TPP/RGO nanocomposite.[27]

Glassy Carbon Electrode Modification. Glassy carbon electrode (GCE) was polished by an alumina polisher (particle size 0.05 μm) and cleaned with DI water. Mn-TPP/RGO (2 mg) was dispersed in 1 mL of DMF, and 5 μL of the

suspension was drop casted on the GCE and air-dried to obtain the Mn-TPP//RGO/GCE electrode.[38] The optical image of the fabricated electrode is shown in Figure S1. RGO/GCE, TPP/GCE, Mn-TPP/GCE, TPP/RGO/GCE, and Mn-TPP/RGO/GCE electrodes were also prepared in the same way.

RESULTS AND DISCUSSION

Characterization. XRD spectra for graphene oxide (GO) and reduced graphene oxide (RGO) are depicted in Figure S2. An intense peak for GO was observed at 10.5° that corresponded to the (001) plane, and the RGO peak shift toward right at 26.5° corresponded to the (002) plane, indicating the removal of oxygen functionalities. The small peak at 44.3° along the (101) plane reflected unoxidized graphite. The gradual broadness in the peak was attributed to exfoliation in reduced graphene oxide due to vigorous reducing conditions. As the reaction time is increased and the reaction conditions intensify, the exfoliation is also increased. The applied forces overcame the interlayer $\pi-\pi$ interactions between stacked graphite layers and separated them, which are evident from the XRD spectrum.[39]

Absorbance spectra of the compounds were recorded with UV−vis spectroscopy using DMF as solvent as shown in Figure 1 and Figure S3. GO showed two characteristic bands in
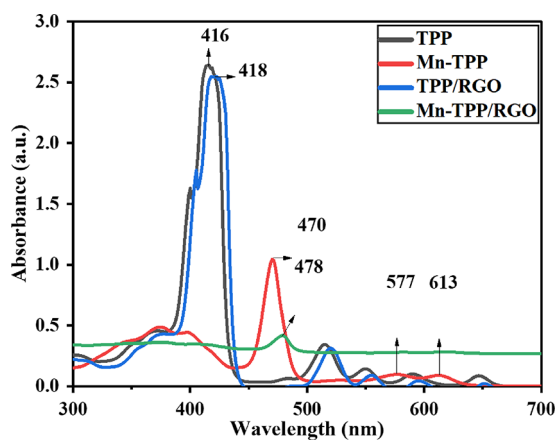

Figure 1. UV/vis analysis of TPP, Mn-TPP, TPP/RGO, and Mn-TPP/RGO.

the UV region. The prominent band at 237 nm is attributed to $\pi \rightarrow \pi^*$ transition that resulted from the presence of C=C, and the shoulder band at 307 nm was due to n $\rightarrow \pi^*$ transition that resulted from the existence of nonbonding electrons over the oxygen atom in carbonyl (−C=O) groups of graphene oxide.[40] The band observed at 289 nm for RGO represented the $\pi \rightarrow \pi^*$ transition due to C=C. In comparison, RGO showed absorption peak at higher wavelength (289 nm) than GO (237 nm) due to the extended conjugation and delocalization of the electronic cloud in RGO; this shows the reduction of GO into RGO.[27] TPP exhibited a prominent Soret band at 416 nm attributed to the strong absorption of the $\pi \rightarrow \pi^*$ transition and Q bands at 515, 549, 590, and 647 nm due to some weak absorptions. The UV−visible spectrum of Mn-TPP exhibited a shift in the absorption of Soret band at 470 nm, and the number of Q bands was reduced to two, which appeared at 576 and 613 nm.[41] The TPP/RGO nanocomposite exhibited the Soret band at 418 nm and the

respective Q bands with a slight shift. Mn-TPP/RGO also displayed a corresponding Soret band at 478 nm with a bathochromic shift due to $\pi \rightarrow \pi^*$ interaction between manganese tetraphenylporphyrin and reduced graphene oxide.

The prepared compounds and the composites were additionally analyzed by FTIR as depicted in Figure 2. All
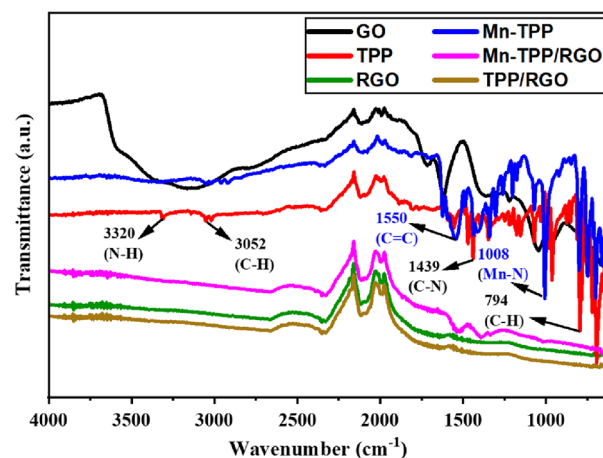

Figure 2. FTIR analysis of GO, Mn-TPP, TPP, Mn-TPP/RGO, RGO, and TPP/RGO.

materials were analyzed in the powder state without any preliminary treatment. In the case of RGO oxygen functionality, bands were not observed, which confirm the reduction GO. Tetraphenylporphyrin (TPP) exhibited the absorption bands at 794, 940, 1342, 1439, 1558, 3052, and 3350 cm^{-1} due to C−H bend, N−H bend, C−N, C=N, C=C, C−H, and secondary N−H stretching vibrations.[42] Mn-TPP displayed absorption bands at 798, 1005, 1331, 1440, 1550, and 3040 cm^{-1} for the C−H bending vibrations, Mn−N (manganese-porphyrin nitrogen bond), C−N, C=N, C=C, and C−H stretching vibrations. The absence of N−H stretching band at 3350 cm^{-1} and N−H bending vibration at 940 cm^{-1} in Mn-TPP confirmed the successful metalation of TPP.[41] Mn-TPP/RGO showed corresponding peaks of Mn-TPP for aromatic C=C, C=N, C−N, and Mn−N stretching vibrations but with slight shifting. These absorption bands confirmed the successful $\pi \rightarrow \pi^*$ interaction between RGO and Mn-TPP.

SEM analysis was performed to determine the morphology of RGO, TPP/RGO, and Mn-TPP/RGO nanocomposites, and results are demonstrated in Figure 3a,b and Figure S4a. SEM analysis of RGO showed a wrinkled structure. Exfoliated RGO formed a crumpled structure.[43] EDS analysis of RGO in Figure 3c showed the elemental composition for carbon (90%) and oxygen (10%). The TPP/RGO nanocomposite (Figure S4b) displayed carbon (96%) and oxygen (4%) in its elemental composition. EDS analysis for Mn-TPP/RGO in Figure 3d showed the presence of manganese (3%), carbon (82%), and oxygen (15%), which indicated the formation of the composite.

Electrochemical Impedance Spectroscopy. Charge transferability of the nanocomposite modified electrodes at the electrolyte−electrode interface was estimated by EIS analysis. Figure 4a presents the EIS response of bare GCE, TPP, Mn-TPP, RGO, TPP/RGO, and Mn-TPP/RGO in 0.5 mM potassium ferricyanide solution in the frequency range of 100 kHz to 0.1 Hz at an AC voltage of 10 mVrms and applied potential of 0.6 V. All the EIS experiments were conducted
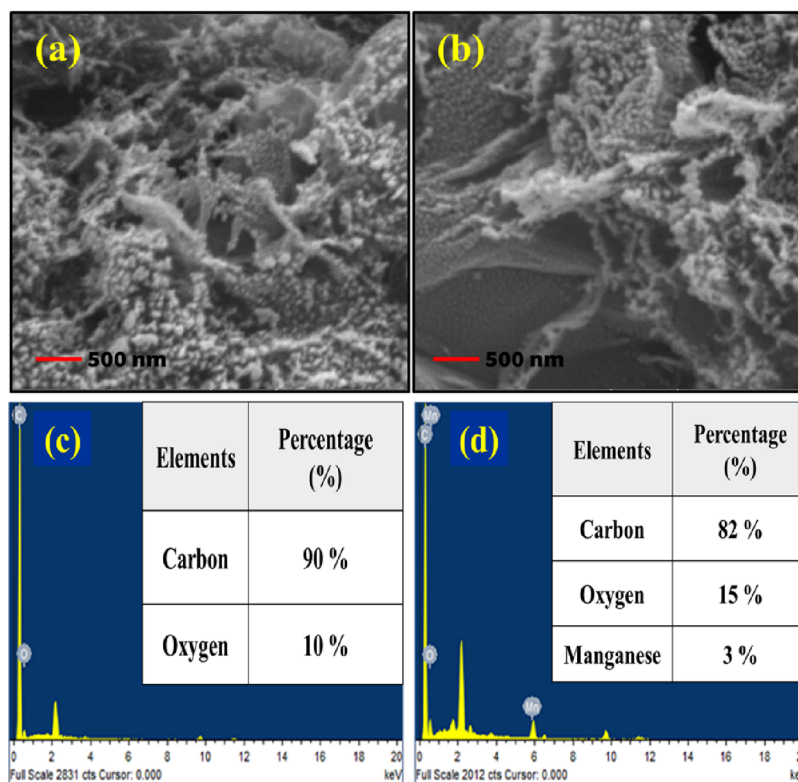
Figure 3. SEM analysis of (a) RGO and (b) Mn-TPP/RGO. EDS analysis of (c) RGO and (d) Mn-TPP/RGO.
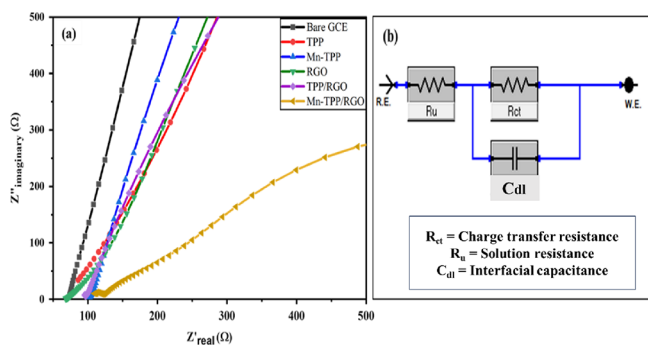

Figure 4. (a) EIS analysis of bare GCE, TPP, Mn-TPP, RGO TPP/RGO, and Mn-TPP/RGO in 0.5 mM potassium ferricyanide solution and (b) Randles electrical circuit.

under open circuit potential. The typical Nyquist plot shows two zones; first, the half circle zone shows resistance in transfer of charge (R_{ct}) for the electrodes, and a linear region displays the diffusion-controlled process. Randles circuit (Figure 4b) was applied on all the electrodes. The Randles circuit includes the charge transfer resistance (R_{ct}) obtained from the semicircles, solution resistance (R_u) of the electrolyte also known as the electrolyte ohmic resistance, and the capacitance of the interface (C_{dl}). For this study, we can estimate the conductivity of the fabricated electrode by considering the value of the charge transfer resistance experienced by electrodes. Table S1 presents the values for the electron transfer resistance (R_{ct}) for different modified electrode systems. The Mn-TPP/RGO modified electrode presented a lower R_{ct} value of 722.9 (ohm) as compared to other electrode systems owing to noncovalent stacking interactions among RGO and Mn-TPP that increase the surface area and henceforth the electrocatalytic property of the electrode; this

shows the good electron transfer capability and high electrical conductivity of the Mn-TPP/RGO electrode.

Electroactive Surface Area of Electrodes. The electroactive surface area of different modified electrodes (bare GCE, TPP, Mn-TPP, RGO, TPP/RGO, and Mn-TPP/RGO) was determined by performing cyclic voltammetry in 0.5 mM $K_3[Fe(CN)_6]$ and 0.1 M phosphate buffer solution (Figure S5). The effective surface area of the electrodes was calculated by using the Randles−Sevcik equation[33,44] as given below:

$$I_p = 2.69 \times 10^5 \times A \times D^{1/2} \times v^{1/2} \times n^{3/2} \times C_0 \qquad (3)$$

where I_p represents the peak current in amperes; A designates the effective surface area (ESA); D is the distribution coefficient of the redox probe $[Fe(CN)_6]^{-3/-4}$, i.e., 7.6×10^{-6} cm^2 s^{-1}; v represents the scan rate in V/s; n designates the number of electrons; and C_0 refers to the concentration of $[Fe(CN)_6]^{-3/-4}$ in mol/L. The ESAs of bare GCE, TPP, Mn-TPP, RGO, TPP/RGO, and Mn-TPP/RGO were found to be 0.37, 0.10, 0.16, 0.15, 0.39, and 0.43 cm^2, respectively. These values indicate an increased electrocatalytic surface area of Mn-TPP by the successful intercalation of RGO.

Electrochemical Behavior of Modified Electrodes. Cyclic voltammetry (CV) was used at different modified electrode systems, i.e., bare GCE, RGO/GCE, TPP/GCE, Mn-TPP/GCE, TPP/RGO/GCE, and Mn-TPP/RGO/GCE, in 0.1 M PBS (pH 3) for 0.5 mM DOX at the scan rate of 50 mVs^{-1}, whereas the range of potential was maintained between −1.0 and +1.0 V. GCE modified with the nanocomposite was used as the working electrode, Ag/AgCl was used as the reference electrode, and platinum wire was used as the auxiliary electrode. Because of the presence of quinone and hydroquinone functionalities, DOX exhibited excellent electroactivity. Electrochemical oxidation of DOX is a two-electron

transfer process as shown in Scheme S3.[45] It was observed that the Mn-TPP/RGO electrode showed the highest peak current response among all of the prepared electrodes, as shown in Figure 5. It demonstrated an anodic peak current (I_{pa}) of 40.77
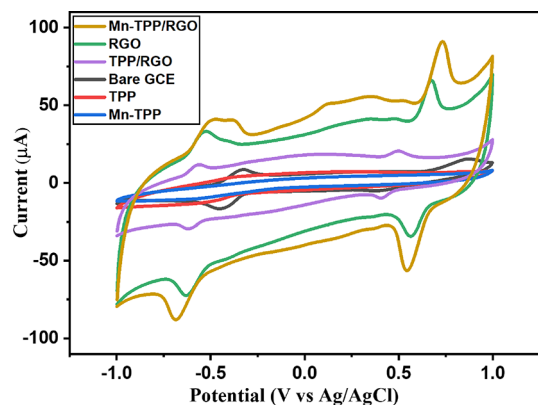

Figure 5. CV at Mn-TPP/RGO, RGO, TPP/RGO, bare GCE, TPP, and Mn-TPP for 0.5 mM DOX in 0.1 M PBS (pH 3) at a scan rate of 50 mV s^{-1}.

μA at −0.47 V for the quinone group and 92.59 μA at 0.73 V for the HQ group. It was due to its elevated charge transferability, superior electrocatalytic activity, and excellent conductivity, so it is used as advanced electrode material for the detection of DOX.

At Different pH Values. The effect of pH plays a substantial role in the electrochemical study of DOX. The electrochemical studies of the Mn-TPP/RGO modified electrode for 0.5 mM DOX in 0.1 M PBS of pH 3 to 7 were performed by CV at 50 mV s^{-1} as shown in Figure 6a. As we increased the pH from 3 to 7, the peak current for quinone and hydroxyquinone groups gradually decreased. The peak current for pH 3 and 5 was contradictory as the quinone group exhibited the highest peak current at pH 5 whereas the hydroquinone group showed the highest peak current at pH 3. This could be due to the complete solubility of DOX at pH 3, whereas it was observed to precipitate out at pH 5. A shift in peak position of the hydroquinone group was also observed with the increase of pH from 3 to 7. It might be due to the meager availability of H$^+$ in the electrochemical redox reaction of the hydroquinone group.[32] Thus, pH 3 was considered the optimum pH for electrocatalytic studies of DOX. The linear

regression equation (eq 4) was obtained from the calibration curve of the hydroquinone group plotted between the anodic peak potential (E_{pa}) and pH (Figure 6b), which is

$$E_{pa} (V) = 0.088 (pH) + 1.032 (R^2 = 0.88) \tag{4}$$

The theoretical value of the Nernst equation is 0.059 V/pH, which explains that an equal number of protons and electrons is involved in the electro-oxidation reaction. The value of the slope is −0.088 V/pH (eq 2), which is close to −0.059, suggesting that two protons and two electrons are involved in the electro-oxidation of DOX.

Effect of Variable Sweep Rate (v). The electrochemical performance of Mn-TPP/RGO/GCE for 0.5 mM DOX (0.1 M PBS, pH 3) was observed at different scan rates. Anodic and cathodic peak currents for both the quinone and hydroquinone groups were increased by increasing the scan rate from 5 to 150 mV s^{-1}. A linear relationship was observed between anodic and cathodic peak current with the square root of the scan rate ($v^{1/2}$) as shown in Figure 7a,b. Thus, it showed that the electrochemical reaction of DOX is a diffusion-controlled method.[46] It is because of the increased charge transfer rate between DOX and the modified electrode as the composite material provided a large surface area and, as a result, a large peak current was observed.[32] The linear regression equation for anodic and cathodic peak current of HQ group can be expressed as

$$I_{pa} = 25.13v^{1/2} - 58.40 \text{ for which } R^2 = 0.99 \tag{5}$$

$$I_{pc} = -13.18v^{1/2} + 32.61 \text{ for which } R^2 = 0.98 \tag{6}$$

When the redox peak current was plotted against the scan rate as shown in Figure S6a, a linear trend (eqs 7 and 8) was obtained that shows the existence of an adsorption-controlled process at the surface of the electrode. Herein, the values of R^2 in eqs 7 and 8 are equal to 0.99 and greater than those obtained in eqs 5 and 6. Thus, the process of DOX detection using Mn-TPP/RGO/GCE is an adsorption-controlled process, which is confirmed later.

$$I_{pa} = 1.77v + 16.13 \text{ for which } R^2 = 0.99 \tag{7}$$

$$I_{pc} = -0.94v - 11.23 \text{ for which } R^2 = 0.99 \tag{8}$$

Further, the kinetics of the redox reaction was confirmed by the plot of the logarithmic relationship of the redox current
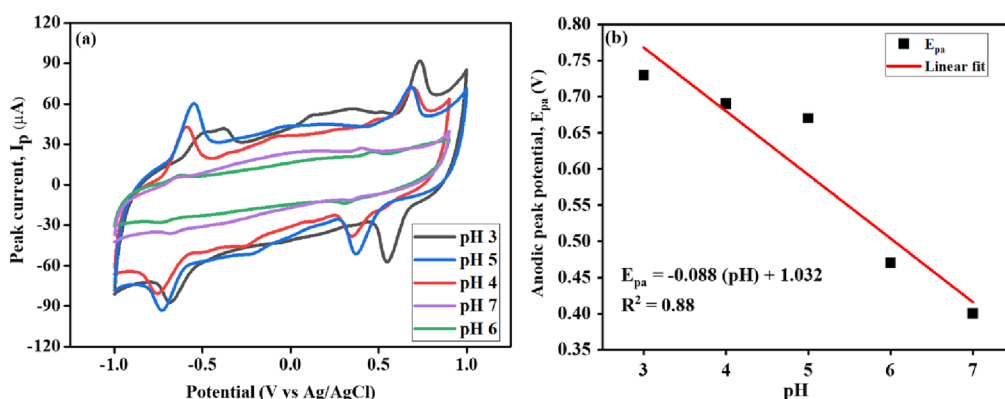

Figure 6. (a) CV response for DOX (0.5 mM) at the Mn-TPP/RGO modified electrode using pH solutions from 3 to 7 and (b) calibration curve between pH and E$_{pa}$.
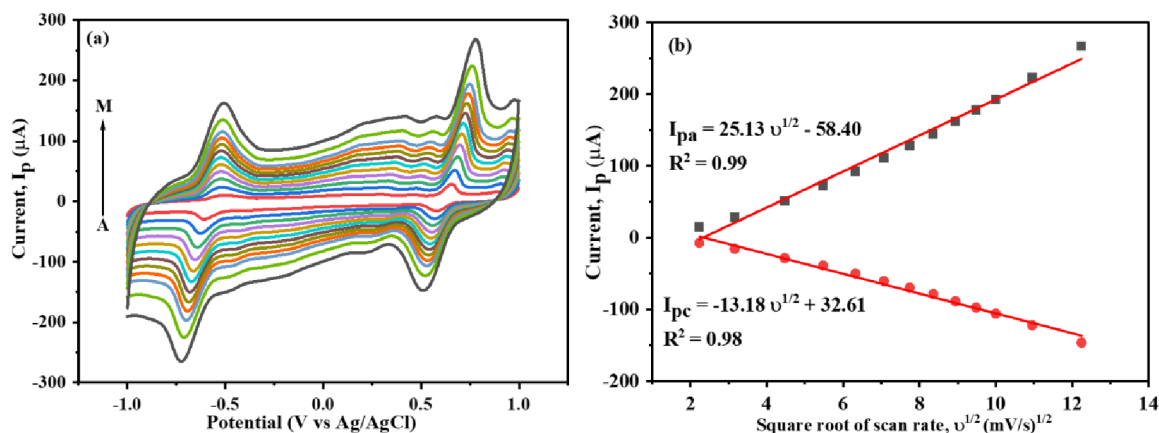
Figure 7. (a) CV at the Mn-TPP/RGO modified electrode at various scan rates (A to M: 5,10, 20, 30, 40, 50, 60, 70, 80, 90,100, 120, and 150 mV s^{-1}) for 0.5 mM DOX (in 0.1 M PBS, pH 3) and (b) calibration curve of $v^{1/2}$ vs peak current.
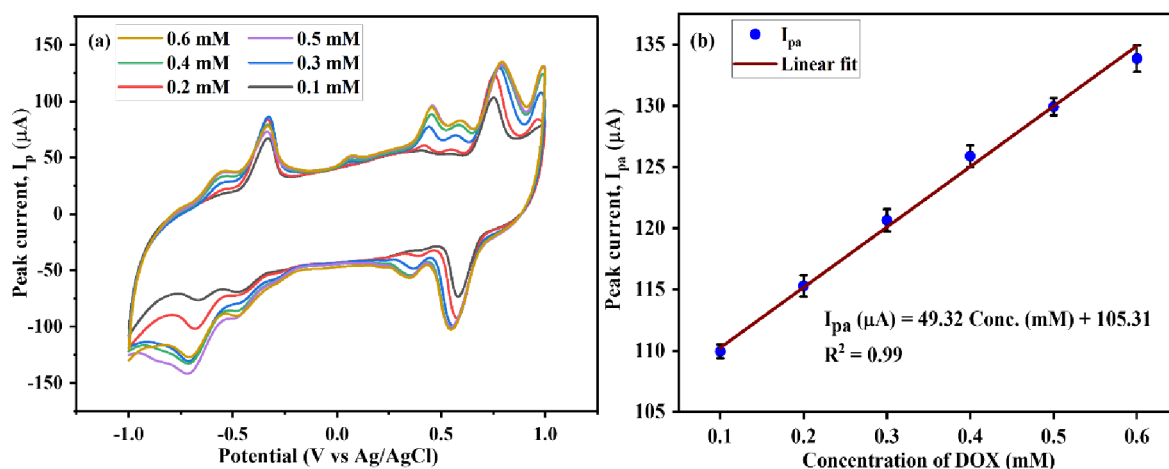

Figure 8. Cyclic voltammogram of the Mn-TPP/RGO electrode for the various concentrations of DOX and (b) calibration plot for different concentration values of DOX vs peak current.
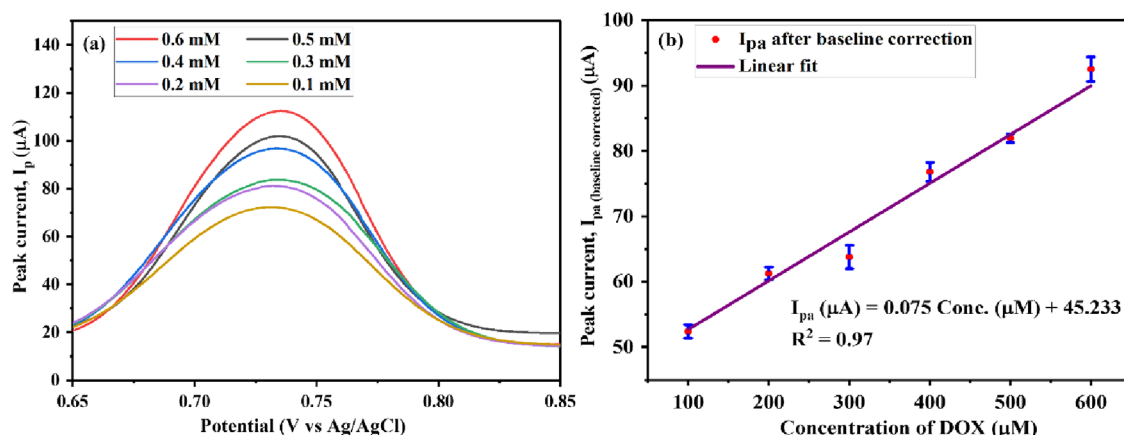

Figure 9. (a) DPV analysis of the Mn-TPP/RGO electrode for the various concentrations of DOX and (b) calibration plot for the different concentration values of DOX vs peak current.

versus scan rate, and the slope obtained was 0.82 (Figure S6b) for both oxidation and reduction peaks, and it depicts that the electro-redox process of DOX at the surface of the Mn-TPP/RGO/GCE electrode is adsorption controlled. The peak potential was also dependent on scan rate. The oxidation peak potential (E_{pa}) was somewhat shifted to a more positive potential, whereas the reduction peak potential (E_{pc}) was

somewhat shifted toward a more negative potential with increasing scan rate as depicted in Figure 7a. It confirmed that the electrochemical redox mechanism of DOX is a quasi-reversible process as the ratio of I_{pa}/I_{pc} is greater than 1.[47]

Effect of Different Concentrations at DPV and CV. CV and DPV were performed at an Mn-TPP/RGO modified electrode to analyze the effect of various concentration values
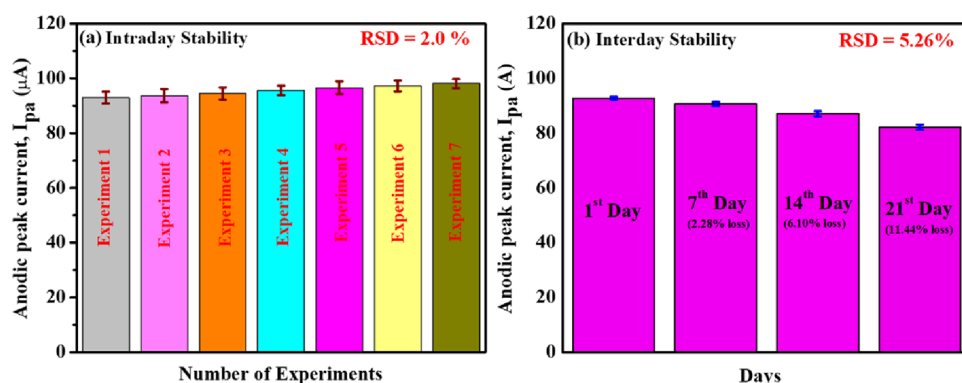
Figure 10. Bar graphs of (a) intraday stability (repeatability analysis) and (b) interday stability of the Mn-TPP/RGO modified electrode for 0.5 mM DOX in 0.1 M PBS of pH 3.

of DOX (0.1 M PBS, pH 3) at the scan rate of 50 mV s^{-1}. Increased peak current was observed in the cyclic voltammogram for DOX as concentration was increased from 100 to 600 mM, which indicates the increased rate of diffusion at the surface of the electrode[48] as shown in Figure 8a,b. CV also depicted the limit of detection (LoD), limit of quantification (LoQ), and sensitivity, which are 63.5 μM, 211.0 μM, and 112.09 μA mM^{-1} cm^{-2}, respectively.

DPV was also performed to analyze the response of the modified electrode toward increased concentration, and results are depicted in Figure 9a,b. Peak current increased as concentration increased from 0.1 to 0.6 mM, whereas peak potential remained unchanged at 0.74 V. Further, the baseline correction of the DPV data was performed by taking the difference between the peak current for each concentration ($I_{concentration}$) and the blank reading current (I_{blank}), i.e., $I_{concentration} - I_{blank}$. The calibration plot for DPV studies with baseline correction is shown in Figure 9b. LoD, LoQ, and sensitivity were 27 μM, 89.9 μM, and 0.174 μA μM^{-1} cm^{-2}, respectively.

Selectivity, Stability, Reproducibility, and Repeatability. DPV was performed for selectivity studies of doxorubicin. It was analyzed by adding interfering agents in 3-fold higher concentration than the concentration of DOX in 0.1 M PBS (pH 3). KCl, NaHCO$_3$, MgSO$_4$, glucose, uric acid, ascorbic acid, leucine, and glycine were used as interfering agents and analyzed individually in the DOX solution. There was no significant change observed in peak potential as well as peak current, and no additional oxidation peak for KCl, NaHCO$_3$, MgSO$_4$, glucose, uric acid, ascorbic acid, leucine, and glycine was observed in the potential window of 0.65 to 0.85 V as clearly shown in Figure S7a,b. Mn-TPP/RGO/GCE showed no interaction with these interferents. Thus, the Mn-TPP/RGO modified electrode has demonstrated −2.7% tolerance for KCl, −4.5% tolerance for NaHCO$_3$, −1.9% tolerance for MgSO$_4$, −0.21% tolerance for glucose, +3.7% tolerance for ascorbic acid, −0.43% tolerance for leucine, −4.3% tolerance for glycine, and −5.1% tolerance for uric acid, as shown in Table S2. The electrocatalytic response of Mn-TPP/RGO/GCE, observed in the potential range of 0.65 to 0.85 V with DOX oxidation at pH 3, is likely a result of the effective binding between DOX and the Mn ion in Mn-TPP. Consequently, interfering compounds did not exhibit interaction with the manganese ion. It depicted the good selectivity and specificity of the synthesized sensor for DOX.

Moreover, seven repetitive measurements were carried out on the Mn-TPP/RGO/GCE electrode for 0.5 mM DOX in 0.1 M PBS (pH 3), and the percentage relative standard deviation (%RSD) was calculated to be 2.0% as shown in Figure 10a. In addition to that, an interday stability study was also done on Mn-TPP/RGO for sensing of DOX. The synthesized electrode was stored in a refrigerator for 21 days, and the CV was done after every 7 days. A total of 2.28, 6.10, and 11.44% signal losses were observed after 7, 14, and 21 days, respectively, which indicated the excellent stability of the sensor with %RSD of 5.26% as shown in Figure 10b.

The Mn-TPP/RGO modified GCE electrode also showed excellent reproducibility with %RSD of 1.46% for three repetitive measurements that were carried out by three different electrodes as shown in Figure 11.
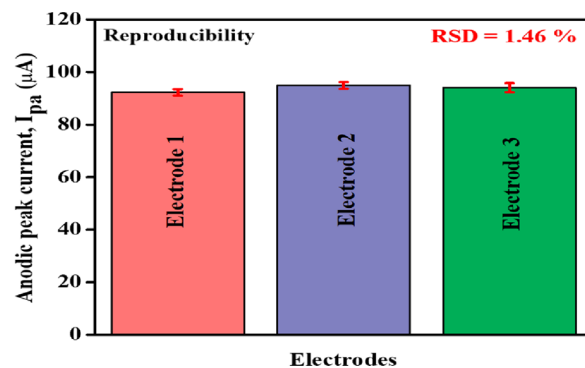

Figure 11. Bar graph for three different Mn-TPP/RGO modified electrodes for 0.5 mM DOX in 0.1 M PBS (pH 3).

Real Sample Analysis. The Mn-TPP/RGO/GCE sensor was also employed in human serum for the detection of DOX, and it exhibited excellent recovery. Serum was separated from the blood sample of a healthy person. Different amounts (20, 30, 40, and 50 μM) of DOX were added in the serum (10 mL) using the standard addition method. Then the serum solution was added to PBS (0.1M, pH 3) for further analysis. Cyclic voltammetry (CV) was performed to measure the current with the addition of DOX. The current exhibited by these concentrations in the serum was compared with the calibration curve of concentrations in the buffer solution, and the percentage (%) recovery along with relative standard deviation values (RSD %; $n = 3$) was calculated as shown in Table 1.

Table 1. Real Sample Analysis Was Performed in Human Serum Using Mn-TPP/RGO/GCE

sr. no.	added (μM)	found (μM)	recovery (%)	relative standard deviation (RSD %)
1	20	21	105%	±1.71
2	30	28	93%	±5.13
3	40	39	97.5%	±2.09
4	50	48	96%	±2.66

Comparison with the Literature. The synthesized sensor was also compared with the literature as shown in Table S3. Mn-TPP/RGO depicted comparable results with better sensitivity as compared to the fabricated systems in sr. nos. 2, 3, and 4 and lower as compared to sr. no. 1, as mentioned in Table S3. Furthermore, it is an easy-to-synthesize and cost-effective sensor as compared to other sensors reported in the literature.

CONCLUSIONS

In conclusion, RGO was prepared successively by chemical reduction of GO along with successive metalation of TPP. TPP/RGO and Mn-TPP/RGO nanocomposites were synthesized by $\pi \rightarrow \pi$ stacking interaction between RGO and porphyrin substrates for successful electrochemical detection of doxorubicin, which were further confirmed and characterized by FTIR, UV/visible spectroscopy, XRD, SEM, and EDS. CV, DPV, and EIS were performed for electrochemical determination of DOX. Mn-TPP/RGO exhibited excellent results for 0.5 mM DOX (0.1 M PBS, pH 3) at a scan rate of 50 mV s^{-1} with a peak current of 92.59 μA at 0.74 V. The prepared sensor exhibited a linear response range from 0.1 to 0.6 mM with LOD of 63.5 μM, LOQ of 211.0 μM, and sensitivity of 112.09 μA mM^{-1} cm^{-2}. In DPV, it exhibited a constant peak potential of about 0.74 V. Moreover, it showed excellent stability, repeatability, sensitivity, and reproducibility. Hence, the electrode modified as Mn-TPP/RGO/GCE sensor can be used reliably for the detection of DOX.

ASSOCIATED CONTENT

ⓢ Supporting Information

The Supporting Information is available free of charge at https://pubs.acs.org/doi/10.1021/acsomega.3c09026.

> Synthesis scheme of TPP; synthesis scheme of Mn-TPP; electrochemical oxidation of DOX; optical image of the Mn-TPP/RGO/GCE fabricated electrode; XRD spectra of GO and RGO; UV/vis analysis of GO and RGO; SEM and EDS analysis of TPP/RGO; cyclic voltammetric analysis of bare GCE, TPP, Mn-TPP, RGO, TPP/RGO, and Mn-TPP/RGO in 0.5 mM potassium ferricyanide solution; calibration graphs of (a) scan rate vs redox current and (b) logarithmic relationship of scan rate versus anodic peak current; DPV studies of the selectivity of Mn-TPP/RGO/GCE toward DOX in the presence of (a) inorganic compounds and (b) biomolecules commonly present in the blood serum; statistical data of EIS analysis of modified electrodes in 0.5 mM potassium ferricyanide solution; data of selectivity studies for Mn-TPP/RGO/GCE toward DOX; and comparison of working ability of Mn-TPP/ RGO/GCE with electrodes present in the literature for the detection of DOX (PDF)

AUTHOR INFORMATION

Corresponding Author

Habib Nasir − *School of Natural Sciences (SNS), National University of Sciences and Technology (NUST), Islamabad 44000, Pakistan;* ◉ orcid.org/0000-0002-9850-2230; Email: habibnasir@sns.nust.edu.pk

Authors

Rafia Zafar − *School of Natural Sciences (SNS), National University of Sciences and Technology (NUST), Islamabad 44000, Pakistan*

Syeda Aqsa Batool Bukhari − *School of Natural Sciences (SNS), National University of Sciences and Technology (NUST), Islamabad 44000, Pakistan*

Complete contact information is available at:
https://pubs.acs.org/10.1021/acsomega.3c09026

Notes

The authors declare no competing financial interest.

ACKNOWLEDGMENTS

REFERENCES

(1) Lima, H. R. S.; da Silva, J. S.; de Oliveira Farias, E. A.; Teixeira, P. R. S.; Eiras, C.; Nunes, L. C. C. Electrochemical sensors and biosensors for the analysis of antineoplastic drugs. *Biosens. Bioelectron.* **2018**, *108*, 27−37.

(2) Fouladgar, M. CuO-CNT nanocomposite/ionic liquid modified sensor as new breast anticancer approach for determination of doxorubicin and 5-fluorouracil drugs. *J. Electrochem. Soc.* **2018**, *165* (13), B559.

(3) Corrie, P. G. Cytotoxic chemotherapy: clinical aspects. *Medicine* **2008**, *36* (1), 24−28.

(4) Ahn, M.-J.; Lee, K.-H.; Ahn, J.-I.; Yu, D.-H.; Lee, H.-S.; Choi, J.-H.; Jang, J. S.; Bae, J. M.; Lee, Y.-S. The differential gene expression profiles between sensitive and resistant breast cancer cells to adriamycin by cDNA microarray. *Cancer research and treatment: official journal of Korean Cancer Association* **2004**, *36* (1), 43.

(5) Liu, Y.-Y.; Hill, R. A.; Li, Y.-T. Ceramide glycosylation catalyzed by glucosylceramide synthase and cancer drug resistance. *Advances in cancer research* **2013**, *117*, 59−89.

(6) van der Zanden, S. Y.; Qiao, X.; Neefjes, J. New insights into the activities and toxicities of the old anticancer drug doxorubicin. *FEBS J.* **2020**, *288*, 6095.

(7) El-Agamy, S. E.; Abdel-Aziz, A. K.; Wahdan, S.; Esmat, A.; Azab, S. S. Astaxanthin ameliorates doxorubicin-induced cognitive impairment (chemobrain) in experimental rat model: impact on oxidative, inflammatory, and apoptotic machineries. *Molecular neurobiology* **2018**, *55* (7), 5727−5740.

(8) Lai, Y.-L.; Cheng, Y.-M.; Yen, S.-K. Doxorubicin-chitosan-hydroxyapatite composite coatings on titanium alloy for localized cancer therapy. *Materials Science and Engineering: C* **2019**, *104*, No. 109953.

(9) Ehsani, M.; Soleymani, J.; Mohammadalizadeh, P.; Hasanzadeh, M.; Jouyban, A.; Khoubnasabjafari, M.; Vaez-Gharamaleki, Y. Low potential detection of doxorubicin using a sensitive electrochemical sensor based on glassy carbon electrode modified with silver nanoparticles-supported poly (chitosan): A new platform in pharmaceutical analysis. *Microchemical Journal* **2021**, *165*, No. 106101.

(10) Zienkiewicz-Strzałka, M.; Deryło-Marczewska, A.; Skorik, Y. A.; Petrova, V. A.; Choma, A.; Komaniecka, I. Silver nanoparticles on

chitosan/silica nanofibers: Characterization and antibacterial activity. *International journal of molecular sciences* **2020**, *21* (1), 166.

(11) Monneret, C. Recent developments in the field of antitumour anthracyclines. *European journal of medicinal chemistry* **2001**, *36* (6), 483−493.

(12) Boucek, R. J.; Steele, A.; Miracle, A.; Atkinson, J. Effects of angiotensin-converting enzyme inhibitor on delayed-onset doxorubicin-induced cardiotoxicity. *Cardiovascular toxicology* **2003**, *3* (4), 319−329.

(13) Schenone, A. V.; Culzoni, M. J.; Campiglia, A. D.; Goicoechea, H. C. Total synchronous fluorescence spectroscopic data modeled with first-and second-order algorithms for the determination of doxorubicin in human plasma. *Anal. Bioanal. Chem.* **2013**, *405* (26), 8515−8523.

(14) Alhareth, K.; Vauthier, C.; Gueutin, C.; Ponchel, G.; Moussa, F. HPLC quantification of doxorubicin in plasma and tissues of rats treated with doxorubicin loaded poly (alkylcyanoacrylate) nanoparticles. *Journal of Chromatography B* **2012**, *887*, 128−132.

(15) Yang, X.; Gao, H.; Qian, F.; Zhao, C.; Liao, X. Internal standard method for the measurement of doxorubicin and daunorubicin by capillary electrophoresis with in-column double optical-fiber LED-induced fluorescence detection. *J. Pharm. Biomed. Anal.* **2016**, *117*, 118−124.

(16) Fojta, M.; Fojtová, M.; Havran, L.; Pivoňková, H.; Dorčák, V.; Šestáková, I. Electrochemical monitoring of phytochelatin accumulation in Nicotiana tabacum cells exposed to sub-cytotoxic and cytotoxic levels of cadmium. *Anal. Chim. Acta* **2006**, *558* (1−2), 171−178.

(17) Schwartz, H. S. A fluorometric assay for daunomycin and adriamycin in animal tissues. *Biochemical medicine* **1973**, *7* (3), 396−404.

(18) Guo, H.; Jin, H.; Gui, R.; Wang, Z.; Xia, J.; Zhang, F. Electrodeposition one-step preparation of silver nanoparticles/carbon dots/reduced graphene oxide ternary dendritic nanocomposites for sensitive detection of doxorubicin. *Sens. Actuators, B* **2017**, *253*, 50−57.

(19) Jin, H.; Guo, H.; Gao, X.; Gui, R. Selective and sensitive electrochemical sensing of gastrodin based on nickel foam modified with reduced graphene oxide/silver nanoparticles complex-encapsulated molecularly imprinted polymers. *Sens. Actuators, B* **2018**, *277*, 14−21.

(20) Fei, J.; Wen, X.; Zhang, Y.; Yi, L.; Chen, X.; Cao, H. Voltammetric determination of trace doxorubicin at a nano-titania/nafion composite film modified electrode in the presence of cetyltrimethylammonium bromide. *Microchimica acta* **2009**, *164* (1), 85−91.

(21) Kochmann, S. *Graphene as a sensor material*. 2014.

(22) Javed, K.; Krumme, A.; Viirsalu, M.; Krasnou, I.; Plamus, T.; Vassiljeva, V.; Tarasova, E.; Savest, N.; Mere, A.; Mikli, V.; Danilson, M.; Kaljuvee, T.; Lange, S.; Yuan, Q.; Topham, P. D.; Chen, C.-M. A method for producing conductive graphene biopolymer nanofibrous fabrics by exploitation of an ionic liquid dispersant in electrospinning. *Carbon* **2018**, *140*, 148−156.

(23) Biesaga, M.; Pyrzyńska, K.; Trojanowicz, M. Porphyrins in analytical chemistry. A review. *Talanta* **2000**, *51* (2), 209−224.

(24) Gross, A. J.; Bucher, C.; Coche-Guerente, L.; Labbé, P.; Downard, A. J.; Moutet, J.-C. Nickel (II) tetraphenylporphyrin modified surfaces via electrografting of an aryldiazonium salt. *Electrochemistry communications* **2011**, *13* (11), 1236−1239.

(25) Suijkerbuijk, B. M.; Klein Gebbink, R. J. Merging porphyrins with organometallics: synthesis and applications. *Angew. Chem., Int. Ed.* **2008**, *47* (39), 7396−7421.

(26) Sakthinathan, S.; Kubendhiran, S.; Chen, S.-M.; Tamizhdurai, P. Reduced graphene oxide/gold tetraphenyl porphyrin (RGO/Au−TPP) nanocomposite as an ultrasensitive amperometric sensor for environmentally toxic hydrazine. *RSC Adv.* **2016**, *6* (61), 56375−56383.

(27) Karuppiah, C.; Sakthinathan, S.; Chen, S. M.; Manibalan, K.; Chen, S. M.; Huang, S. T. A non-covalent functionalization of copper tetraphenylporphyrin/chemically reduced graphene oxide nanocomposite for the selective determination of dopamine. *Appl. Organomet. Chem.* **2016**, *30* (1), 40−46.

(28) Sakthinathan, S.; Lee, H. F.; Chen, S.-M.; Tamizhdurai, P. Electrocatalytic oxidation of dopamine based on non-covalent functionalization of manganese tetraphenylporphyrin/reduced graphene oxide nanocomposite. *J. Colloid Interface Sci.* **2016**, *468*, 120−127.

(29) Sakthinathan, S.; Kubendhiran, S.; Chen, S. M.; Manibalan, K.; Govindasamy, M.; Tamizhdurai, P.; Huang, S. T. Reduced Graphene Oxide Non-covalent Functionalized with Zinc Tetra Phenyl Porphyrin Nanocomposite for Electrochemical Detection of Dopamine in Human Serum and Rat Brain Samples. *Electroanalysis* **2016**, *28* (9), 2126−2135.

(30) van Staden, J. F.; Stefan-van Staden, R. I. Application of porphyrins in flow-injection analysis: A review. *Talanta* **2010**, *80* (5), 1598−1605.

(31) Francisco, M. S. P.; Cardoso, W. S.; Kubota, L. T.; Gushikem, Y. Electrocatalytic oxidation of phenolic compounds using an electrode modified with Ni (II) porphyrin adsorbed on SiO2/Nb2O5-phosphate synthesized by the sol−gel method. *J. Electroanal. Chem.* **2007**, *602* (1), 29−36.

(32) Bukhari, S. A. B.; Nasir, H.; Pan, L.; Tasawar, M.; Sohail, M.; Shahbaz, M.; Gul, F.; Sitara, E. Supramolecular assemblies of carbon nanocoils and tetraphenylporphyrin derivatives for sensing of catechol and hydroquinone in aqueous solution. *Sci. Rep.* **2021**, *11* (1), 5044.

(33) Aqsa Batool Bukhari, S.; Nasir, H.; Sitara, E.; Akhtar, T.; Ramazan Oduncu, M.; Iram, S.; Pan, L. Efficient electrochemical detection of dopamine with carbon nanocoils and copper tetra(p-methoxyphenyl)porphyrin nanocomposite. *Arabian J. Chem.* **2022**, *15* (12), No. 104375.

(34) Adler, A. D.; Longo, F. R.; Finarelli, J. D.; Goldmacher, J.; Assour, J.; Korsakoff, L. A simplified synthesis for meso-tetraphenylporphine. *Journal of Organic Chemistry* **1967**, *32* (2), 476−476.

(35) Boakye, A.; Yu, K.; Asinyo, B. K.; Chai, H.; Raza, T.; Xu, T.; Zhang, G.; Qu, L. A Portable Electrochemical Sensor Based on Manganese Porphyrin-Functionalized Carbon Cloth for Highly Sensitive Detection of Nitroaromatics and Gaseous Phenol. *Langmuir* **2022**, *38* (39), 12058−12069.

(36) Zaaba, N.; Foo, K.; Hashim, U.; Tan, S.; Liu, W.-W.; Voon, C. Synthesis of graphene oxide using modified hummers method: solvent influence. *Procedia engineering* **2017**, *184*, 469−477.

(37) Park, S.; An, J.; Potts, J. R.; Velamakanni, A.; Murali, S.; Ruoff, R. S. Hydrazine-reduction of graphite-and graphene oxide. *Carbon* **2011**, *49* (9), 3019−3023.

(38) Bukhari, S. A. B.; Nasir, H.; Pan, L.; Tasawar, M.; Sohail, M.; Shahbaz, M.; Gul, F.; Sitara, E. Supramolecular assemblies of carbon nanocoils and tetraphenylporphyrin derivatives for sensing of catechol and hydroquinone in aqueous solution. *Sci. Rep.* **2021**, *11* (1), 5044.

(39) Stobinski, L.; Lesiak, B.; Malolepszy, A.; Mazurkiewicz, M.; Mierzwa, B.; Zemek, J.; Jiricek, P.; Bieloshapka, I. Graphene oxide and reduced graphene oxide studied by the XRD, TEM and electron spectroscopy methods. *J. Electron Spectrosc. Relat. Phenom.* **2014**, *195*, 145−154.

(40) Xu, S.; Yong, L.; Wu, P. One-pot, green, rapid synthesis of flowerlike gold nanoparticles/reduced graphene oxide composite with regenerated silk fibroin as efficient oxygen reduction electrocatalysts. *ACS Appl. Mater. Interfaces* **2013**, *5* (3), 654−662.

(41) Ezzayani, K.; Ben Khelifa, A.; Saint-Aman, E.; Loiseau, F.; Nasri, H. Complex of hexamethylenetetramine with magnesium-tetraphenylporphyrin: Synthesis, structure, spectroscopic characterizations and electrochemical properties. *J. Mol. Struct.* **2017**, *1137*, 412−418.

(42) Qian-Kun, Z.; Gao, X.-X. The voltammetric behavior of water-soluble ytterbium porphyrin complex in aqueous media. *Electrochimica acta* **1995**, *40* (8), 959−964.

(43) Ates, M.; Özten, E. The comparison of capacitor behaviors of polymethylcarbazole and polymethylcarbazole/graphene. *J. Alloys Compd.* **2017**, *714*, 433−442.

(44) Wang, M.; Lin, J.; Gong, J.; Ma, M.; Tang, H.; Liu, J.; Yan, F. Rapid and sensitive determination of doxorubicin in human whole blood by vertically-ordered mesoporous silica film modified electrochemically pretreated glassy carbon electrodes. *RSC Adv.* **2021**, *11* (15), 9021−9028.

(45) Deepa, S.; Kumara Swamy, B. E.; Vasantakumar Pai, K. Voltammetric detection of anticancer drug Doxorubicin at pencil graphite electrode: A voltammetric study. *Sens. Int.* **2020**, *1*, No. 100033.

(46) Radhakrishnan, S.; Krishnamoorthy, K.; Sekar, C.; Wilson, J.; Kim, S. J. A promising electrochemical sensing platform based on ternary composite of polyaniline−Fe2O3−reduced graphene oxide for sensitive hydroquinone determination. *Chemical Engineering Journal* **2015**, *259*, 594−602.

(47) Guo, Y.; He, D.; Xie, A.; Qu, W.; Tang, Y.; Zhou, L.; Zhu, R. The electrochemical oxidation of hydroquinone and catechol through a novel poly-geminal dicationic ionic liquid (PGDIL)−TiO2 composite film electrode. *Polymers* **2019**, *11* (11), 1907.

(48) Haque, F.; Rahman, M.; Ahmed, E.; Bakshi, P.; Shaikh, A. A cyclic voltammetric study of the redox reaction of Cu (II) in presence of ascorbic acid in different pH media. *Dhaka University Journal of Science* **2013**, *61* (2), 161−166.